Journal of Asian Earth Sciences 192 (2020) 104235

Contents lists available at ScienceDirect

Journal of Asian Earth Sciences

journal homepage: www.elsevier.com/locate/jseaes

# Zircon U–Pb geochronology and Sr–Nd–Hf–O isotope geochemistry of Late Jurassic granodiorites in the southern Qiangtang block, Tibet: Remelting of ancient mafic lower crust in an arc setting?

Peng Sun[a,b], Wei Dan[a,c], Qiang Wang[a,b,c,*], Gong-Jian Tang[a,c,*], Quan Ou[a,b], Lu-Lu Hao[a,b], Zi-Qi Jiang[d]

[a] State Key Laboratory of Isotope Geochemistry, Guangzhou Institute of Geochemistry, Chinese Academy of Sciences, Guangzhou 510640, China
[b] University of Chinese Academy of Sciences, Beijing 100049, China
[c] CAS Center for Excellence in Tibetan Plateau Earth Sciences (CETES), Beijing 100101, China
[d] School of Earth Science, Guilin University of Technology, Guilin 541004, China

ARTICLE INFO

*Keywords:*
Granodiorite
Petrogenesis
Late Jurassic
Bangong–Nujiang Tethyan Ocean
Southern Qiangtang Block
Tibet

ABSTRACT

A Late Jurassic–Late Cretaceous magmatic belt extends for > 800 km along the southern margin of the southern Qiangtang Block (SQB) in central Tibet. However, the Mesozoic tectonic setting of these igneous rocks remains uncertain. Here, we report new *in situ* zircon U–Pb ages and Hf–O isotopes as well as whole-rock major- and trace-element compositions and Sr–Nd isotopes for the Jiacuo granodiorites and dikes in the SQB. Zircon laser ablation–inductively coupled plasma–mass spectrometry U–Pb dating indicates that these rocks were emplaced during the Late Jurassic (ca. 153–151 Ma). All of the rocks have high $SiO_2$ (64.7–68.4 wt%) and $K_2O$ (4.2–5.2 wt %) contents and are characterized by enrichment in light rare-earth elements ($(La/Yb)_N$ = 16–19) and large-ion lithophile elements, and depletion in high-field-strength elements. The granodiorites and dikes have variable zircon Hf–O isotope values ($\varepsilon_{Hf}(t)$ = −15.7 to −10.1, $\delta^{18}O$ = +5.32‰ to +7.88‰), but uniform and high whole-rock initial $^{87}Sr/^{86}Sr$ isotopic (0.7079 to 0.7080) and low $\varepsilon_{Nd}(t)$ (−7.9 to −7.6) values. We suggest that these granodiorites were originated by partial melting of ancient mafic lower crust of the SQB. Combining our new data with the temporal and spatial distributions of Mesozoic magmatic rocks in the SQB, we propose that Late Jurassic magmatism in the SQB was resulted from northward subduction of the Bangong–Nujiang Tethyan oceanic slab during this period.

## 1. Introduction

The Tibetan Plateau has undergone multiple convergence events between various blocks since the early Paleozoic (Metcalfe et al., 2013; Zhu et al., 2013). The Qiangtang Block is located in the central Tibetan Plateau, and paleontological, paleomagnetic, and sedimentary characteristics indicate that this block was originated from the northern margin of Gondwana, subsequently migrated northward, and finally accreted to the southern margin of Eurasia (Jin, 2002; Metcalfe et al., 2002, 2013; Zhu et al., 2013). Multiple magmatic and metamorphic events caused by subduction–accretion, arc–continent collision, and continent–continent collision are recorded in the Qiangtang Block (Dan et al., 2018; Zhai et al., 2011, 2013; Zhang et al., 2012; Zhu et al., 2016), meaning that investigation of this block should provide insights into the evolution of the Tethys Ocean and the formation of the Tibetan Plateau during the Paleozoic–Mesozoic.

The Qiangtang Block has been divided into the southern Qiangtang Block (SQB) and the northern Qiangtang Block along the Longmu–Shuanghu Suture (LSS) (Fig. 1a) (Dan et al., 2018a, b; Li et al., 1995; Zhai et al., 2011; Zhang et al., 2006; Zhang et al., 2016). Late Mesozoic magmatism in the SQB has attracted much research attention, partly because of the large number of related metallogenic deposits (Li et al., 2012, 2013, 2015, 2016b, 2018). However, the origins of these igneous rocks and the tectonic setting of the SQB during the late Mesozoic remain disputed (Hao et al., 2016a, b, 2018; Li et al., 2014b; Ma et al., 2017; Zhang et al., 2014; Zhu et al., 2011, 2016). A magmatic belt consisting of Late Jurassic and Late Cretaceous granitoids with minor mafic intrusive rocks, basalt, andesite, and dacite extends

* Corresponding authors at: State Key Laboratory of Isotope Geochemistry (SKLaBIG), Guangzhou Institute of Geochemistry (GIG), Chinese Academy of Sciences (CAS), Wushan Street, Guangzhou 510640, China.
*E-mail addresses:* wqiang@gig.ac.cn (Q. Wang), tanggj@gig.ac.cn (G.-J. Tang).

https://doi.org/10.1016/j.jseaes.2020.104235
Received 19 July 2019; Received in revised form 6 January 2020; Accepted 8 January 2020
Available online 29 January 2020

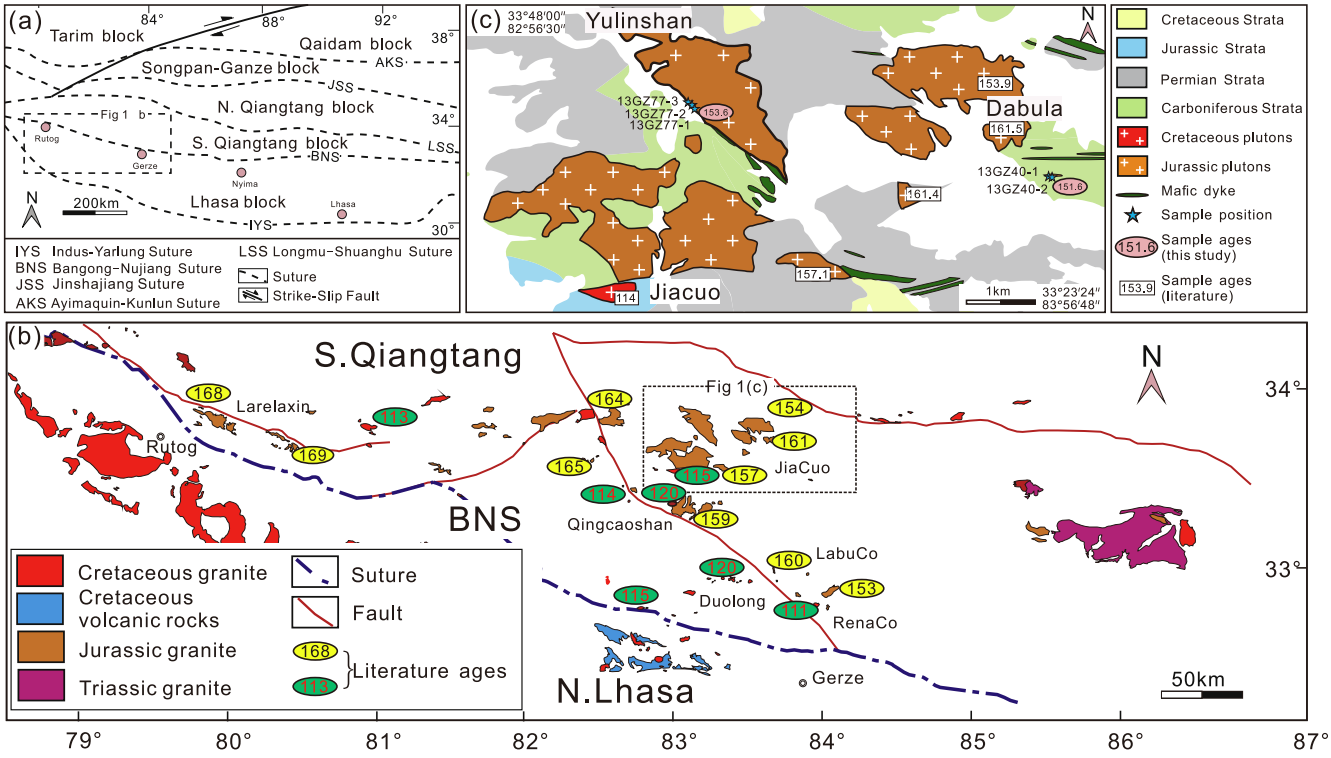


**Fig. 1.** (a) Tectonic framework of the Tibetan Plateau (modified from Chung et al., 2005; Yin and Harrison, 2000). Main suture zones between the major blocks: AKMS – Ayimaqen–Kunlun–Mutztagh Suture; JS – Jinsha Suture; BNS – Bangong–Nujiang Suture; IYS – Indus–Yalu Suture. (b) Map of the central Tibetan Plateau showing the distribution of late Mesozoic igneous rocks in the western SQB. (c) Simplified geologic map showing outcrops of plutons in the Jiacuo area, SQB, central Tibet. Literature age data are from Hao et al. (2016a), Li et al. (2013, 2014a, b, 2015), and Wu et al. (2016).

for > 800 km along the southern part of the SQB (Geng et al., 2016; Hao et al., 2016a, b, 2018; Li et al., 2012, 2013, 2014a, b, 2015, 2016a, b; Liu et al., 2014a; Wu et al., 2016). This belt has been considered as the product of northward subduction of the Bangong–Nujiang Tethyan oceanic plate. The origin of this belt can be constrained from the evolution of the Bangong–Nujiang Tethyan Ocean. There are three main views on the closure age of this ocean: Middle Jurassic (Ma et al., 2017), Early Cretaceous (Zhu et al., 2011, 2016), and late Early Cretaceous (Hao et al., 2016a, b, 2018; Li et al., 2014b; Zhang et al., 2014). Some studies have suggested that the Bangong–Nujiang Tethyan Ocean closed around the Middle Jurassic, based mainly on analyses of sediments and structures (e.g., Ma et al., 2017). Other studies, on the basis of Hf isotope data and the spatiotemporal distribution of magmatism in the northern Lhasa Block, have suggested that the marked change in zircon $\varepsilon_{Hf}(t)$ values at ca. 110 Ma records tectonomagmatic activity resulting from slab break-off following closure of the Bangong–Nujiang Tethyan Ocean (ca. 130–120 Ma) (Zhu et al., 2011, 2016). The most recent studies have proposed that the Bangong–Nujiang Tethyan Ocean survived until the late Early Cretaceous on the basis of magmatism, metallogenesis, deformation, and the presence of ophiolitic mélange in the Bangong–Nujiang Suture (e.g., Hao et al., 2016a, b, 2018; Li et al., 2014b; Zhang et al., 2014).

The widely distributed igneous rocks of the SQB provide an opportunity to better constrain the evolution of the Bangong–Nujiang Tethyan Ocean during the late Mesozoic. Here, we present combined petrological, zircon U–Pb geochronological and Hf–O isotopic, and whole-rock major- and trace-element and Sr–Nd isotope data for Late Jurassic granodiorites in the Jiacuo area of the SQB. We infer from the results that these granodiorites were generated by partial melting of ancient mafic lower crust of the SQB as a result of northward subduction of the Bangong–Nujiang Tethyan oceanic plate during the Late Jurassic.

## 2. Geological setting and rock types

From north to south, the Tibetan Plateau comprises a series of independent blocks, namely the Kunlun–Qaidam, Songpan–Ganzi–Hoh Xil, Qiangtang, Lhasa, and Himalaya blocks, separated by four major sutures (Fig. 1a) (Chung et al., 2005; Yin and Harrison, 2000). The Qiangtang Block is located in central Tibet and is bounded by the Jinsha Suture (JS) to the north and the Bangong–Nujiang Suture (BNS) to the south (Chung et al., 2005). The Bangong–Nujiang Suture Zone (BNSZ), which is the boundary between the SQB and the Lhasa block, extends for 1700 km in central Tibet. The BNSZ is composed of Jurassic–-Cretaceous flysch, mélange, and scattered Early–Middle Jurassic ophiolitic fragments that represent remnants of the Bangong–Nujiang ocean (Kapp et al., 2003).

Previous studies have suggested that metasedimentary and metavolcanic rocks in the Duguer (Kapp et al., 2000; Pullen et al., 2011), Gangma Co (Kapp et al., 2000), and Rongma (Zhao et al., 2014) areas in the SQB represent Precambrian to early Paleozoic continental basement. The SQB comprises Ordovician–Devonian metasedimentary rocks

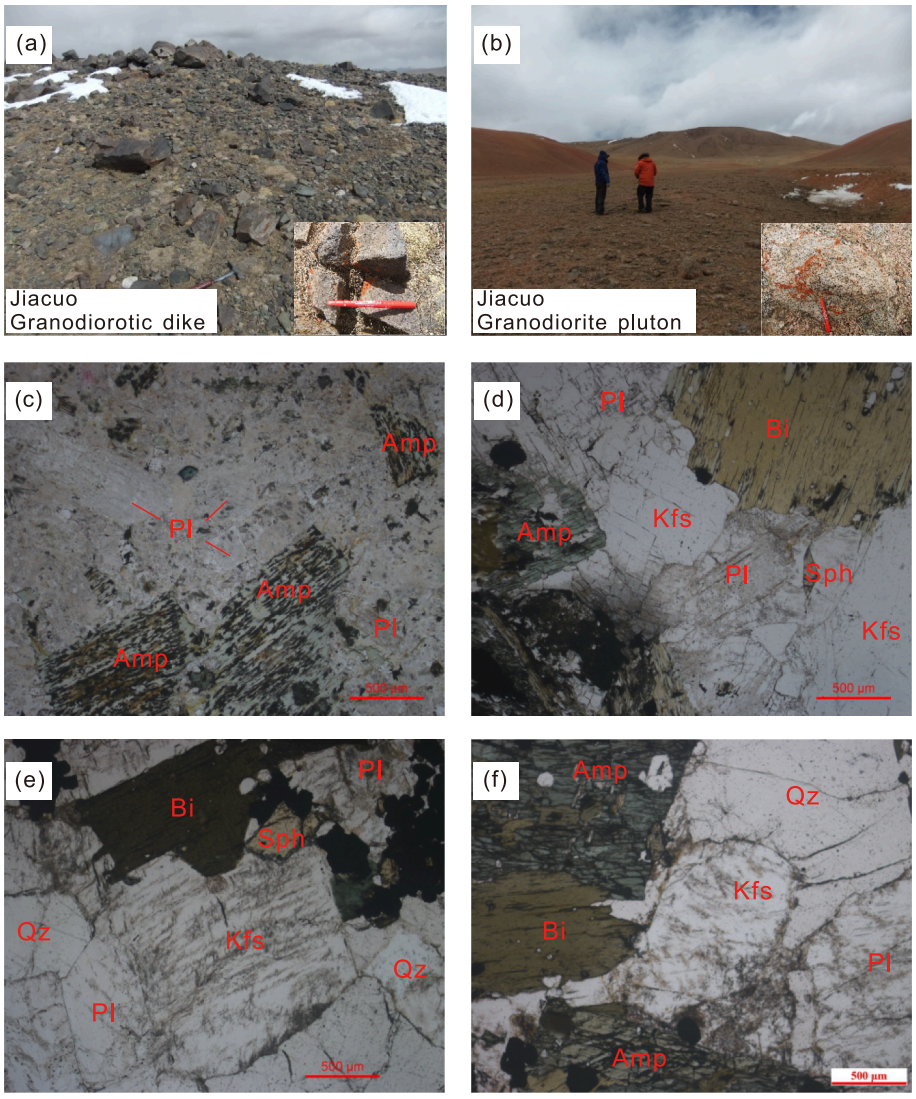


**Fig. 2.** Field outcrops and photomicrographs of the Jiacuo granodioritic rocks. (a) Granodioritic dikes in eastern Jiacuo and a hand specimen (inset). (b) Granodioritic pluton in western Jiacuo and hand specimen (inset). (c) Sample 13GZ40-1 (granodioritic dike) showing porphyritic texture. The phenocrysts are plagioclase and amphibole, and have been altered. (d–e) Sample 13GZ77-1 (granodiorite pluton) and (f) sample 13GZ77-2 (granodiorite pluton) showing euhedral amphibole and biotite with interstitial subhedral–anhedral plagioclase. Abbreviations: Pl = plagioclase. Amp = amphibole, Kfs = K-feldspar, Bi = biotite, Qz = quartz, Sph = sphene.

and sandy limestones, Carboniferous–Permian clastic sedimentary rocks (including sandstone, shale, and limestone), and interbeds of conglomerate, volcanic rocks, Triassic limestones, and Jurassic sandstones and limestones (Metcalfe, 2013; Zhu et al., 2016).

Late Mesozoic magmatic rocks (169–90 Ma) are widely distributed in the SQB from the Rutog area in the west to the Dongqiao and Anduo areas in the east (Geng et al., 2016; Hao et al., 2016a, b; Li et al., 2012, 2013, 2014a, b, 2015, 2016a, b; Liu et al., 2014a; Wu et al., 2016; Zhu et al., 2016). The earliest magmatic rocks, recording northward subduction of Bangong–Nujiang Tethyan oceanic slab under the SQB, are Jurassic granites of the Larelaxin and Caima plutons (~168 Ma) (Li et al., 2014b). The Jurassic magmatic rocks are distributed mainly in the southern margin and central part of the SQB. The northernmost Jurassic pluton is located ~170 km from the Bangong–Nujiang suture zone. Some Cretaceous igneous rocks also occur in the SQB. The distance between the northernmost Cretaceous magmatic rocks and the Bangong–Nujiang suture zone is about 70 km (Fig. 1b).

The Jiacuo pluton and dikes, which are mainly granodioritic, are intruded into upper Carboniferous and lower Permian strata in the northernmost part of the late Mesozoic magmatic belt. Granodiorites in the western part of the pluton contain plagioclase (45–50 vol%), K-feldspar (~10 vol%), quartz (~20 vol%), and biotite and amphibole (10–15 vol%) with accessory zircon, apatite, titanite, and Fe–Ti oxides. Granodiorite dikes in the eastern part of the pluton contain plagioclase (30–35 vol%), K-feldspar (~10 vol%), quartz (~25 vol%), amphibole (5–10 vol%), and biotite (~15 vol%) with accessory zircon, apatite, titanite, and Fe–Ti oxides (Fig. 2).

## 3. Analytical methods

The least altered samples selected for elemental and isotopic analysis were split into small chips and then powdered to ~200 mesh size in an agate mortar after rinsing with distilled water. The whole-rock major element oxides (wt. %) were analyzed at the State Key Laboratory of Isotope Geochemistry, Guangzhou Institute of Geochemistry, Chinese Academy of Sciences (SKLaBIG, GIGCAS) by

**Table 1**
Major oxide and trace element concentrations of granodiorites from the Jiacuo pluton and dike, Southern Qiangtang block, Tibet.

| Sample | 13GZ40-1 | 13GZ40-2 | 13GZ77-1 | 13GZ77-2 | 13GZ77-3 |
|---|---|---|---|---|---|
| type | granodiorotic dyke | granodiorotic dyke | granodiorite pluton | granodiorite pluton | granodiorite pluton |
| GPS | 83.933°E | 83.933°E | 83.400°E | 83.383°E | 83.367°E |
| | 33.566°N | 33.566°N | 33.583°N | 33.583°N | 33.600°N |
| Age | 151.6 Ma | | 153.3 Ma | | |
| SiO2 | 64.8 | 64.8 | 67.3 | 68.4 | 67.1 |
| TiO2 | 0.72 | 0.68 | 0.50 | 0.45 | 0.47 |
| Al2O3 | 15.0 | 14.9 | 14.7 | 14.4 | 14.8 |
| Fe2O3T | 5.43 | 5.39 | 4.30 | 3.92 | 4.23 |
| MnO | 0.08 | 0.10 | 0.09 | 0.10 | 0.11 |
| MgO | 2.33 | 2.21 | 1.78 | 1.62 | 1.68 |
| CaO | 3.27 | 3.68 | 3.36 | 3.16 | 3.08 |
| Na2O | 3.49 | 3.39 | 3.00 | 2.97 | 2.84 |
| K2O | 4.25 | 4.23 | 4.53 | 4.45 | 5.20 |
| P2O5 | 0.23 | 0.23 | 0.17 | 0.15 | 0.16 |
| LOI | 2.04 | 2.34 | 0.48 | 0.52 | 0.43 |
| Mg# | 48.5 | 47.4 | 47.6 | 47.6 | 46.7 |
| A/CNK | 0.92 | 0.89 | 0.92 | 0.93 | 0.93 |
| Sc | 11.7 | 11.2 | 9.47 | 8.30 | 8.99 |
| V | 107 | 102 | 81.2 | 70.6 | 78.8 |
| Cr | 299 | 328 | 15.8 | 316 | 409 |
| Co | 11.7 | 12.8 | 9.54 | 9.66 | 10.6 |
| Ni | 25.4 | 31.8 | 7.75 | 27.2 | 34.7 |
| Mn | 602 | 814 | 652 | 726 | 843 |
| Cu | 36.1 | 35.6 | 7.15 | 33.1 | 44.5 |
| Zn | 38.9 | 49.4 | 39.5 | 30.0 | 35.1 |
| Ga | 19.5 | 18.6 | 17.6 | 16.1 | 16.4 |
| Ge | 2.25 | 2.24 | 2.06 | 1.86 | 1.96 |
| Cs | 3.59 | 4.40 | 5.83 | 4.28 | 5.56 |
| Rb | 153 | 157 | 214 | 185 | 224 |
| Ba | 870 | 1010 | 504 | 470 | 706 |
| Th | 17.4 | 16.8 | 27.4 | 20.1 | 28.6 |
| U | 4.11 | 4.59 | 3.48 | 3.31 | 3.20 |
| Nb | 16.6 | 15.9 | 20.6 | 16.7 | 18.7 |
| Ta | 1.51 | 1.49 | 2.43 | 1.94 | 2.20 |
| La | 42.2 | 40.7 | 43.8 | 38.7 | 38.4 |
| Ce | 76.9 | 73.5 | 74.9 | 65.6 | 67.0 |
| Pb | 13.5 | 13.7 | 17.4 | 15.7 | 17.9 |
| Pr | 8.76 | 8.29 | 7.87 | 6.79 | 7.21 |
| Sr | 390 | 404 | 415 | 406 | 429 |
| Nd | 31.8 | 30.2 | 27.1 | 23.7 | 25.2 |
| Zr | 166 | 191 | 119 | 112 | 144 |
| Hf | 4.76 | 5.36 | 3.57 | 3.20 | 4.05 |
| Sm | 5.52 | 5.21 | 4.43 | 3.78 | 4.16 |
| Eu | 1.36 | 1.29 | 1.04 | 0.92 | 1.00 |
| Gd | 4.90 | 4.60 | 3.89 | 3.44 | 3.65 |
| Tb | 0.67 | 0.65 | 0.53 | 0.46 | 0.50 |
| Dy | 3.72 | 3.55 | 2.93 | 2.58 | 2.83 |
| Y | 19.1 | 18.3 | 15.8 | 13.7 | 15.1 |
| Ho | 0.74 | 0.71 | 0.60 | 0.53 | 0.57 |
| Er | 2.01 | 1.92 | 1.68 | 1.45 | 1.60 |
| Tm | 0.29 | 0.28 | 0.26 | 0.22 | 0.25 |
| Yb | 1.88 | 1.80 | 1.70 | 1.47 | 1.63 |
| Lu | 0.30 | 0.29 | 0.28 | 0.24 | 0.27 |

standard X-ray fluorescence (XRF) spectrometry with analytical errors better than 3%. Details of the analytical procedures were described by Li et al. (2006). Trace elements were analyzed by inductively coupled plasma mass spectrometry (ICP–MS), using a Perkin–Elmer Sciex ELAN 6000 instrument at the GIGCAS. Analytical procedures are similar to those described by Li et al. (2006). Analytical precisions for most elements are better than 5%. The major and trace element data are listed in Table 1.

Whole-rock Sr, Nd isotope compositions of selected samples were performed using a Micromass Isoprobe multi–collector mass spectrometer (MC–ICPMS) at the SKLaBIG, GIGCAS. Analytical procedures are the same as those described by Li et al. (2006). Measured $^{87}Sr/^{86}Sr$ and $^{143}Nd/^{144}Nd$ ratios were corrected to $^{86}Sr/^{88}Sr = 0.1194$ and $^{146}Nd/^{144}Nd = 0.7219$ respectively. During the period of data acquisition, the $^{87}Sr/^{86}Sr$ ratios of the NBS987 standard are 0.710262 ± 5 (2σ), $^{143}Nd/^{144}Nd$ ratios of the Shin Etsu JNdi-1 standard are 0.512110 ± 3 (2σ). The Sr-Nd isotope data are presented in Table 2.

The conventional heavy liquid and magnetic separation techniques

**Table 2**
Whole rock Sr-Nd isotopic compositions of granodiorites from the Jiacuo pluton and dike, Southern Qiangtang block, Tibet.

| Rock type | Sample | Age (Ma) | Rb | Sr | $^{87}Rb/^{86}Sr$ | $^{87}Sr/^{86}Sr_{(m)}$ | 1SE | $^{87}Sr/^{86}Sr_{(i)}$ | Sm | Nd | $^{147}Sm/^{144}Nd$ | $^{143}Nd/^{144}Nd_{(m)}$ | 1SE | $\varepsilon Nd_{(t)}$ | $T_{DM}$ (Ma) | $T_{DM2}$ (Ma) | $f_{Sm/Nd}$ |
|---|---|---|---|---|---|---|---|---|---|---|---|---|---|---|---|---|---|
| granodiorotic dike | 13GZ40-1 | 152 | 153 | 390 | 1.1342 | 0.712696 | 0.000007 | 0.710255 | 5.52 | 31.8 | 0.1047 | 0.512154 | 0.000007 | −7.66 | 1397 | 1576 | −0.47 |
| granodiorotic dike | 13GZ40-2 | 152 | 157 | 404 | 1.1199 | 0.712494 | 0.000008 | 0.710084 | 5.21 | 30.2 | 0.1039 | 0.512156 | 0.000004 | −7.62 | 1386 | 1571 | −0.47 |
| granodiorite pluton | 13GZ77-1 | 153 | 214 | 415 | 1.4845 | 0.711136 | 0.000011 | 0.707901 | 4.43 | 27.1 | 0.0985 | 0.512144 | 0.000005 | −7.72 | 1336 | 1582 | −0.50 |
| granodiorite pluton | 13GZ77-2 | 153 | 185 | 406 | 1.3127 | 0.710819 | 0.000011 | 0.707958 | 3.78 | 23.7 | 0.0960 | 0.512140 | 0.000005 | −7.75 | 1314 | 1584 | −0.51 |

were used for zircons separated from two rock samples. Those zircon grains were handpicked and sealed in an epoxy resin disk. The JEOL JXA–8100 Superprobe at SKLaBIG, GIGCAS was used to obtain Cathodoluminescence (CL) images of zircons in order to characterize the internal morphology of individual zircons and selecting potential target sites for U–Pb age and Hf–O isotope analyses.

Zircon U–Pb dating subsequently undertaken using an Agilent 7500a quadruple (Q)–ICPMS and a Neptune multi–collector (MC)–ICPMS with a 193 nm excimer ArF laser-ablation system (GeoLas Plus) equipped at the MC–ICPMS laboratory of the Institute of Geology and Geophysics, Chinese Academy of Sciences (IGGCAS) in Beijing, China. The analytical procedures were described in detail in Xie et al. (2008). During the analysis, zircon 91500 was used as the standard (Wiedenbeck et al., 1995) and the standard silicate glass NIST 610 was used to correct the machine, with a beam diameter of 32 μm. The ICPMSDataCal software (Liu et al., 2010) was used to calculate the $^{207}Pb/^{206}Pb$ and $^{206}Pb/^{238}U$ ratios and the methods of the common Pb corrected according to Andersen (2002). The weighted mean U–Pb ages and Concordia plots were processed using the Isoplot/Ex v.3.0 program (Ludwig, 2003). LA–ICP–MS zircon U–Pb isotopic data are presented in Appendix A.

In situ Hf isotope measurements were conducted on a Neptune Plus MC–ICP–MS (Thermo Scientific) on the condition of beam size: 45 μm, laser pulse frequency: 6 Hz at the SKLaBIG, GIGCAS. The zircons that were previously analyzed for U–Pb isotopes were conducted to Lu–Hf isotopic analyses. The analytical methods are similar to those given in Zhang et al. (2014). Twenty-one analyses of the Qinghu zircon during the course of this study yielded a weighted mean of $^{176}Hf/^{177}Hf$ = 0.289934 ± 0.000019 (2SD), which is consistent within errors with the reported value in Li et al. (2010).

Zircon oxygen isotopes were measured using the Cameca IMS–1280 SIMS at the SKLaBIG, GIGCAS. The detailed analytical procedures were similar to those described in Li et al. (2010). The measured oxygen isotopic data were corrected for instrumental mass fractionation (IMF) using the Penglai zircon standard ($\delta^{18}O_{VSMOW}$ = 5.3‰). The internal precision of a single analysis generally was better than 0.2‰ (1σ) for the $^{18}O/^{16}O$ ratio. The external precision, measured by the reproducibility of repeated analyses of Penglai standard, is 0.42‰ (2σ). Nine measurements of the Qinghu zircon standard during the course of this study yielded a weighted mean of $\delta^{18}O$ = 5.3 ± 0.2‰ (2σ), which is consistent within errors with the reported value of 5.3 ± 0.3‰ in Li et al. (2010). Zircon Hf–O isotopic data are listed in Table 3.

## 4. Results

### 4.1. Zircon U–Pb dating results

Zircons were separated from samples of granodiorite dike (13GZ40-1) and granodiorite pluton (13GZ77-1) for laser ablation–inductively coupled plasma–mass spectrometry (LA–ICP–MS) dating. Zircons from the two samples are 80–200 μm long, euhedral to subhedral and prismatic, and have aspect ratios of 2:1 to 3:1. Most grains show high Th/U ratios (0.30–0.63 for 13GZ40-1, 0.40–0.65 for 13GZ77-1) with clear oscillatory zoning, which are characteristics of igneous zircons (Belousova et al., 2002).

Seventeen analyses of zircons from the granodiorite dike sample are concordant and yield a weighted mean $^{206}Pb/^{238}U$ age of 151.6 ± 1.1 Ma (1σ, MSWD = 0.58) (Fig. 3a). Twenty analyses of zircons from the granodiorite sample are concordant and yield a weighted mean $^{206}Pb/^{238}U$ age of 153.3 ± 1.1 Ma (1σ, MSWD = 0.77) (Fig. 3b). Therefore, the dikes and pluton in the Jiacuo area crystallized during the Late Jurassic (153–151 Ma).

### 4.2. Major and trace elements

Granodiorites and dikes in the Jiacuo area have similar $SiO_2$

**Table 3**
Zircon Hf-O data of granodiorites from the Jiacuo pluton and dike, Southern Qiangtang block, Tibet.

| Analysis | T(Ma) | $^{176}Yb/^{177}Hf$ | $^{176}Lu/^{177}Hf$ | $^{176}Hf/^{177}Hf$ | 2σ | $^{176}Hf/^{177}Hf_i$ | $\varepsilon_{Hf}(0)$ | $\varepsilon_{Hf}(t)$ | $T_{DM}$ (Ma) | $T_{DM}^{C}$ (Ma) | $f_{Lu/Hf}$ | $\sigma^{18}O$ | 2SE |
|---|---|---|---|---|---|---|---|---|---|---|---|---|---|
| 13GZ40-1-01 | | | | | | | | | | | | 6.55 | 0.24 |
| 13GZ40-1-02 | | | | | | | | | | | | 7.19 | 0.22 |
| 13GZ40-1-03 | | | | | | | | | | | | 7.38 | 0.18 |
| 13GZ40-1-04 | 149 | 0.02147 | 0.00088 | 0.282394 | 0.000019 | 0.282392 | −13.4 | −10.2 | 1208 | 1846 | −0.97 | 6.41 | 0.26 |
| 13GZ40-1-05 | 149 | 0.01770 | 0.00073 | 0.282396 | 0.000017 | 0.282393 | −13.3 | −10.1 | 1201 | 1843 | −0.98 | 5.32 | 0.37 |
| 13GZ40-1-06 | 153 | 0.01946 | 0.00076 | 0.282375 | 0.000017 | 0.282373 | −14.0 | −10.7 | 1231 | 1884 | −0.98 | 7.32 | 0.23 |
| 13GZ40-1-07 | | | | | | | | | | | | 7.07 | 0.29 |
| 13GZ40-1-08 | 153 | 0.02728 | 0.00113 | 0.282387 | 0.000020 | 0.282383 | −13.6 | −10.4 | 1227 | 1863 | −0.97 | 6.86 | 0.39 |
| 13GZ40-1-09 | 155 | 0.01668 | 0.00064 | 0.282431 | 0.000020 | 0.282429 | −12.1 | −8.7 | 1149 | 1758 | −0.98 | 7.08 | 0.22 |
| 13GZ40-1-10 | | | | | | | | | | | | 6.83 | 0.34 |
| 13GZ40-1-11 | 150 | 0.01651 | 0.00070 | 0.282373 | 0.000019 | 0.282371 | −14.1 | −10.9 | 1232 | 1893 | −0.98 | 6.43 | 0.34 |
| 13GZ40-1-12 | 150 | 0.01864 | 0.00083 | 0.282386 | 0.000025 | 0.282384 | −13.6 | −10.4 | 1217 | 1864 | −0.97 | 6.87 | 0.28 |
| 13GZ40-1-13 | 150 | 0.01335 | 0.00063 | 0.282451 | 0.000017 | 0.282449 | −11.4 | −8.1 | 1122 | 1719 | −0.98 | 6.75 | 0.22 |
| 13GZ40-1-14 | 152 | 0.01225 | 0.00060 | 0.282391 | 0.000017 | 0.282390 | −13.5 | −10.3 | 1203 | 1853 | −0.98 | 7.88 | 0.25 |
| 13GZ40-1-15 | | | | | | | | | | | | 6.51 | 0.18 |
| 13GZ40-1-16 | 152 | 0.02005 | 0.00093 | 0.282362 | 0.000021 | 0.282359 | −14.5 | −11.4 | 1255 | 1921 | −0.97 | 7.50 | 0.22 |
| 13GZ40-1-17 | 150 | 0.01400 | 0.00062 | 0.282404 | 0.000016 | 0.282402 | −13.0 | −9.8 | 1186 | 1823 | −0.98 | 6.92 | 0.20 |
| 13GZ40-1-18 | 152 | 0.02519 | 0.00104 | 0.282394 | 0.000020 | 0.282391 | −13.4 | −10.1 | 1213 | 1844 | −0.97 | 6.58 | 0.22 |
| 13GZ40-1-19 | | | | | | | | | | | | 6.73 | 0.27 |
| 13GZ40-1-20 | 154 | 0.01193 | 0.00057 | 0.282348 | 0.000017 | 0.282346 | −15.0 | −11.6 | 1262 | 1945 | −0.98 | 6.88 | 0.28 |
| 13GZ40-1-21 | 152 | 0.02492 | 0.00105 | 0.282421 | 0.000032 | 0.282418 | −12.4 | −9.2 | 1176 | 1786 | −0.97 | 6.65 | 0.20 |
| 13GZ40-1-22 | 154 | 0.01881 | 0.00084 | 0.282375 | 0.000022 | 0.282372 | −14.0 | −10.8 | 1234 | 1887 | −0.97 | 7.12 | 0.32 |
| 13GZ40-1-23 | 152 | 0.01452 | 0.00060 | 0.282361 | 0.000020 | 0.282360 | −14.5 | −11.2 | 1245 | 1917 | −0.98 | 7.27 | 0.22 |
| 13GZ40-1-24 | 153 | 0.01875 | 0.00080 | 0.282389 | 0.000019 | 0.282386 | −13.6 | −10.3 | 1213 | 1856 | −0.98 | | |
| 13GZ77-1-01 | | | | | | | | | | | | 7.45 | 0.20 |
| 13GZ77-1-02 | 166 | 0.01961 | 0.00075 | 0.282436 | 0.000015 | 0.282434 | −11.9 | −8.6 | 1145 | 1750 | −0.98 | 6.39 | 0.32 |
| 13GZ77-1-03 | 159 | 0.01753 | 0.00081 | 0.282396 | 0.000018 | 0.282394 | −13.3 | −10.0 | 1203 | 1840 | −0.98 | 7.19 | 0.28 |
| 13GZ77-1-04 | 158 | 0.02202 | 0.00084 | 0.282376 | 0.000019 | 0.282374 | −14.0 | −10.7 | 1232 | 1885 | −0.97 | 6.68 | 0.33 |
| 13GZ77-1-05 | 156 | 0.02239 | 0.00088 | 0.282397 | 0.000015 | 0.282395 | −13.3 | −9.7 | 1204 | 1830 | −0.97 | 6.50 | 0.24 |
| 13GZ77-1-06 | | | | | | | | | | | | 6.89 | 0.23 |
| 13GZ77-1-07 | 155 | 0.02688 | 0.00108 | 0.282345 | 0.000015 | 0.282342 | −15.1 | −11.7 | 1283 | 1952 | −0.97 | 6.66 | 0.27 |
| 13GZ77-1-08 | | | | | | | | | | | | 6.61 | 0.21 |
| 13GZ77-1-09 | 154 | 0.02698 | 0.00101 | 0.282367 | 0.000016 | 0.282365 | −14.3 | −11.1 | 1250 | 1905 | −0.97 | 6.67 | 0.18 |
| 13GZ77-1-10 | 153 | 0.02221 | 0.00087 | 0.282377 | 0.000016 | 0.282375 | −14.0 | −10.7 | 1232 | 1883 | −0.97 | 6.47 | 0.24 |
| 13GZ77-1-11 | 153 | 0.06046 | 0.00223 | 0.282411 | 0.000016 | 0.282405 | −12.8 | −9.5 | 1228 | 1812 | −0.93 | 6.32 | 0.26 |
| 13GZ77-1-12 | | | | | | | | | | | | 6.24 | 0.22 |
| 13GZ77-1-13 | 153 | 0.02478 | 0.00099 | 0.282399 | 0.000016 | 0.282397 | −13.2 | −9.9 | 1204 | 1832 | −0.97 | 6.14 | 0.26 |
| 13GZ77-1-14 | 153 | 0.02699 | 0.00114 | 0.282403 | 0.000014 | 0.282400 | −13.1 | −9.8 | 1204 | 1827 | −0.97 | 6.09 | 0.22 |
| 13GZ77-1-15 | 152 | 0.01981 | 0.00080 | 0.282368 | 0.000013 | 0.282365 | −14.3 | −11.0 | 1242 | 1903 | −0.98 | 6.79 | 0.28 |
| 13GZ77-1-16 | 152 | 0.02532 | 0.00102 | 0.282368 | 0.000015 | 0.282365 | −14.3 | −11.0 | 1249 | 1903 | −0.97 | 6.28 | 0.28 |
| 13GZ77-1-17 | 152 | 0.02246 | 0.00089 | 0.282355 | 0.000015 | 0.282352 | −14.8 | −11.5 | 1263 | 1933 | −0.97 | 6.27 | 0.30 |
| 13GZ77-1-18 | 152 | 0.02221 | 0.00088 | 0.282339 | 0.000015 | 0.282337 | −15.3 | −12.1 | 1284 | 1968 | −0.97 | 6.01 | 0.20 |
| 13GZ77-1-19 | 152 | 0.03591 | 0.00137 | 0.282332 | 0.000017 | 0.282328 | −15.6 | −12.4 | 1312 | 1987 | −0.96 | 5.75 | 0.30 |
| 13GZ77-1-20 | 152 | 0.02399 | 0.00099 | 0.282377 | 0.000016 | 0.282374 | −14.0 | −10.7 | 1236 | 1885 | −0.97 | 5.81 | 0.24 |
| 13GZ77-1-21 | 152 | 0.02301 | 0.00093 | 0.282371 | 0.000013 | 0.282369 | −14.2 | −10.9 | 1242 | 1896 | −0.97 | 6.19 | 0.28 |
| 13GZ77-1-22 | 152 | 0.01648 | 0.00065 | 0.282388 | 0.000013 | 0.282386 | −13.6 | −10.3 | 1209 | 1858 | −0.98 | | |
| 13GZ77-1-23 | 152 | 0.02645 | 0.00104 | 0.282377 | 0.000015 | 0.282374 | −14.0 | −10.7 | 1237 | 1884 | −0.97 | | |
| 13GZ77-1-24 | 151 | 0.02431 | 0.00087 | 0.282293 | 0.000016 | 0.282291 | −16.9 | −13.7 | 1349 | 2071 | −0.97 | | |

Corrected formula as follows Chu et al., 2006:
$(^{176}Hf/^{177}Hf)_i = {}^{176}Hf/^{177}Hf - {}^{176}Lu/^{177}Hf * (e^{\lambda T} - 1)$.
$\varepsilon Hf(T) = [(^{176}Hf/^{177}Hf)_{Sample}(T)/(^{176}Hf/^{177}Hf)_{CHUR}(T) - 1] * 10^4$.
$\lambda$(Lu-Hf) = $1.867 * 10^{-11}$ $year^{-1}$.
$(^{176}Hf/^{177}Hf)_{CHUR}(T) = 0.282772–0.0332 * (e^{\lambda T} - 1)$.
$T_{DM} = 1/\lambda * \ln\{1 + [((^{176}Hf/^{177}Hf)_{sample} - (^{176}Hf/^{177}Hf)_{DM})/((^{176}Lu/^{177}Hf)_{sample} - (^{176}Lu/^{177}Hf)_{DM})]\}$.
$T_{DM}^{C}(Hf) = T_{DM} - (T_{DM}-T) * [(f_{CC} - f_S)/(f_{CC} - f_{DM})]$.
$f_{Lu/Hf} = [(^{176}Lu/^{177}Hf)_{sample}/(^{176}Lu/^{177}Hf)_{CHUR}] - 1$.

(64.7–68.4 wt%), $Al_2O_3$ (0.4–0.7 wt%), $Fe_2O_3^T$ (3.9–5.4 wt%), and MgO (1.6–2.3 wt%) contents. They have $K_2O$ contents of 4.2–5.2 wt% and $Na_2O$ contents of 2.8–3.5 wt%, yielding $K_2O/Na_2O$ ratios of 1.2–1.8. All of the samples are characterized by weakly metaluminous features with A/CNK [molar $Al_2O_3/(CaO + Na_2O + K_2O)$] ratios of 0.89–1.00 (Fig. 4a–e). These rocks are enriched in light rare-earth elements (LREEs) and depleted in heavy REEs (HREEs), with $(La/Yb)_n$ = 16–19 and slight negative Eu anomalies (Eu/Eu* = 0.77–0.80). All of the samples are enriched in large-ion lithosphere elements and depleted in high-field-strength elements, and show positive Th–U and negative Nb–Ta–Ti anomalies in a primitive mantle normalized trace-element variation diagram (Fig. 5a, b).

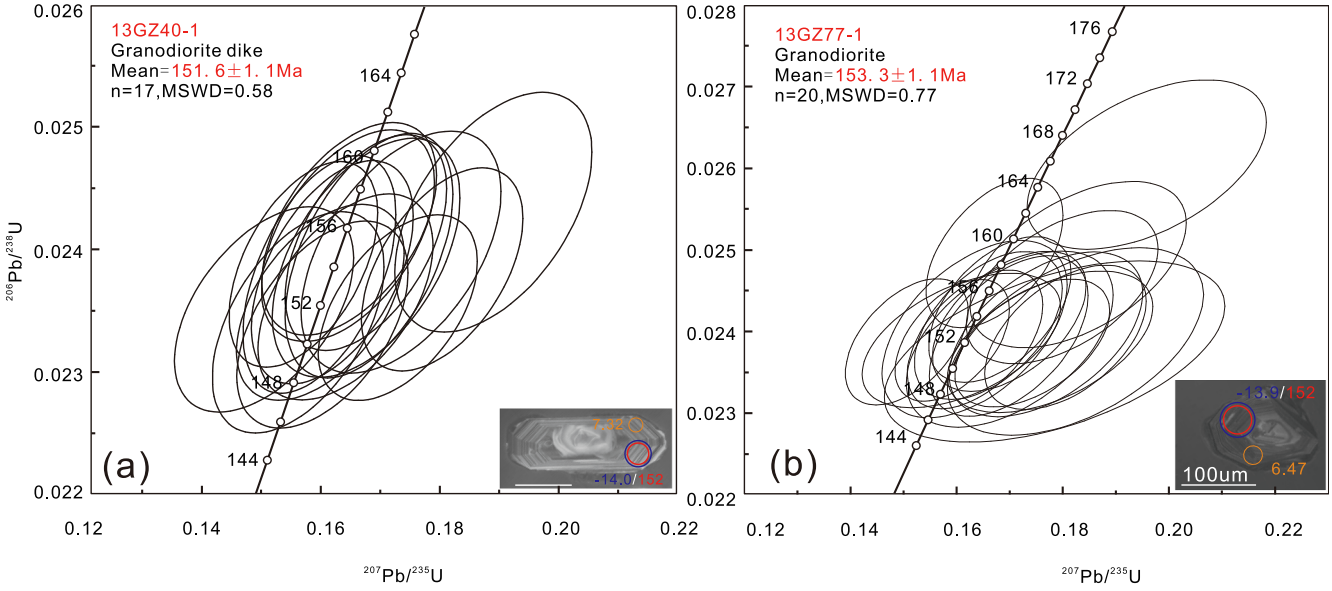


**Fig. 3.** LA–ICP–MS zircon U–Pb concordia diagrams with representative zircon CL images for the Jiacuo granodioritic rocks. (a) Granodioritic dike; (b) granodiorite. Red, yellow, and blue circles and numbers denote the analytical spots and results of U–Pb dating, O isotopes, and Hf isotopes, respectively. (For interpretation of the references to colour in this figure legend, the reader is referred to the web version of this article.)

### 4.3. Whole-rock Sr–Nd and zircon Hf–O isotopes

Sr–Nd isotopes were corrected to 150 Ma in accordance with zircon U–Pb dating results obtained during this study. Granodiorite samples in the Jiacuo area have uniform Sr–Nd isotope compositions (initial $^{87}Sr/^{86}Sr$ = 0.7079 to 0.7080, $\varepsilon_{Nd}(t)$ = − 7.8 to − 7.7), whereas granodiorite dike samples exhibit higher Sr but similar Nd isotope compositions (Fig. 6b, initial $^{87}Sr/^{86}Sr$ = 0.7101 to 0.7102, $\varepsilon_{Nd}(t)$ = −7.7 to −7.6). Granodiorite samples have low LOI (Loss of ignition) contents of 0.4%–0.5%. However, the higher LOI values of granodiorite dike samples (2.0%–2.3%) indicate that the Sr isotope compositions of the dikes may have been affected by alteration. Therefore, only Sr–Nd isotopes of the granodiorites and Nd isotopes of the dikes are used to discuss the petrogenesis of the Jiacuo granodiorites and dikes.

Twenty analyses of the granodiorites yield zircon $\varepsilon_{Hf}(t)$ values of −15.7 to −10.1 (Fig. 6a), and 18 analyses of the granodioritic dikes yield zircon $\varepsilon_{Hf}(t)$ values of −14.6 to −10.0 (Fig. 6a). Twenty-one analyses of the granodiorites yield zircon $\delta^{18}O$ values of 5.8‰ to 7.5‰ (Fig. 7a, mean = 6.5‰ ± 0.4‰), and 23 analyses of the granodioritic dikes indicate more variable zircon $\delta^{18}O$ values of 5.3‰ to 7.9‰ (Fig. 7b, mean = 6.9‰ ± 0.5‰).

## 5. Discussion

### 5.1. Petrogenesis of the Jiacuo granodiorites and dikes

The Jiacuo granodiorites and dikes are metaluminous, calc-alkaline, I-type granitoids, as indicated by the presence of hornblendes (Fig. 2), A/CNK values of < 1.0 (Fig. 4c; A/CNK = 0.9–1.0), and a negative correlation between $SiO_2$ and $P_2O_5$ (Fig. 4d). Several models have been proposed for the petrogenesis of metaluminous, calc-alkaline, I-type granitoids: (1) partial melting of mafic to intermediate igneous sources, including lower crust (ancient or newly formed), subducted oceanic crust, and mélange in the mantle wedge (Altherr et al., 2000; Chappell and White, 2001; Hao et al., 2016; Li et al., 2007; Petford and Atherton, 1996; Wedepohl, 1991); (2) crustal assimilation and fractional crystallization (AFC) of basaltic magmas (Grove et al., 1997; Wu et al., 2003; Yang et al., 2015); and (3) mixing between mantle-derived mafic and crust-derived felsic magmas (Altherr et al., 2000; He et al., 2018; Yu et al., 2018). We propose that the Jiacuo granodiorites and dikes could not have been generated by AFC and magma mixing but were most probably generated by partial melting of ancient crust, as detailed below.

We suggest that the Jiacuo granodiorites and dikes could not have been generated by fractional crystallization of mantle-derived basaltic magmas or mixing between mantle-derived mafic and crust-derived felsic melts, on the basis of the following lines of evidence. (1) Granodiorites in the Jiacuo and adjacent areas are predominantly felsic, and both mafic magma end-member and intermediate rocks are absent (Fig. 4d–h). (2) They have homogeneous whole-rock Sr–Nd (initial $^{87}Sr/^{86}Sr$ isotopic ratios = 0.7078–0.7079, $\varepsilon_{Nd}(t)$ = −7.9 to −7.6) and slightly variable zircon Hf isotope compositions ($\varepsilon_{Hf}(t)$ = −15.7 to −10.0) (Fig. 6a–b), which excludes the possibility of crustal AFC processes of mantle-derived basaltic magmas or mixing between mantle-derived mafic and crust-derived felsic melts. (3) No mafic microgranular enclaves (MMEs) are found in the Jiacuo granodiorites and dikes, which further excludes these rocks having been formed by mixing between mantle-derived mafic and crust-derived felsic melts.

Dehydration melting of basaltic compositions can produce felsic rocks, as shown by experimental petrology studies (Beard and Lofgren, 1991). Intermediate to felsic melts can be generated by dehydration melting of tholeiitic amphibolite (Rapp and Watson, 1995; Rushmer, 1991). However, we suggest that the Jiacuo granodiorites could not have been derived by partial melting of subducted tholeiitic oceanic crust or mélange on the basis of the following lines of evidence. First, the Jiacuo granodiorites and dikes have low $Na_2O/K_2O$ ratios. Petrological experiments have shown that felsic melts produced by

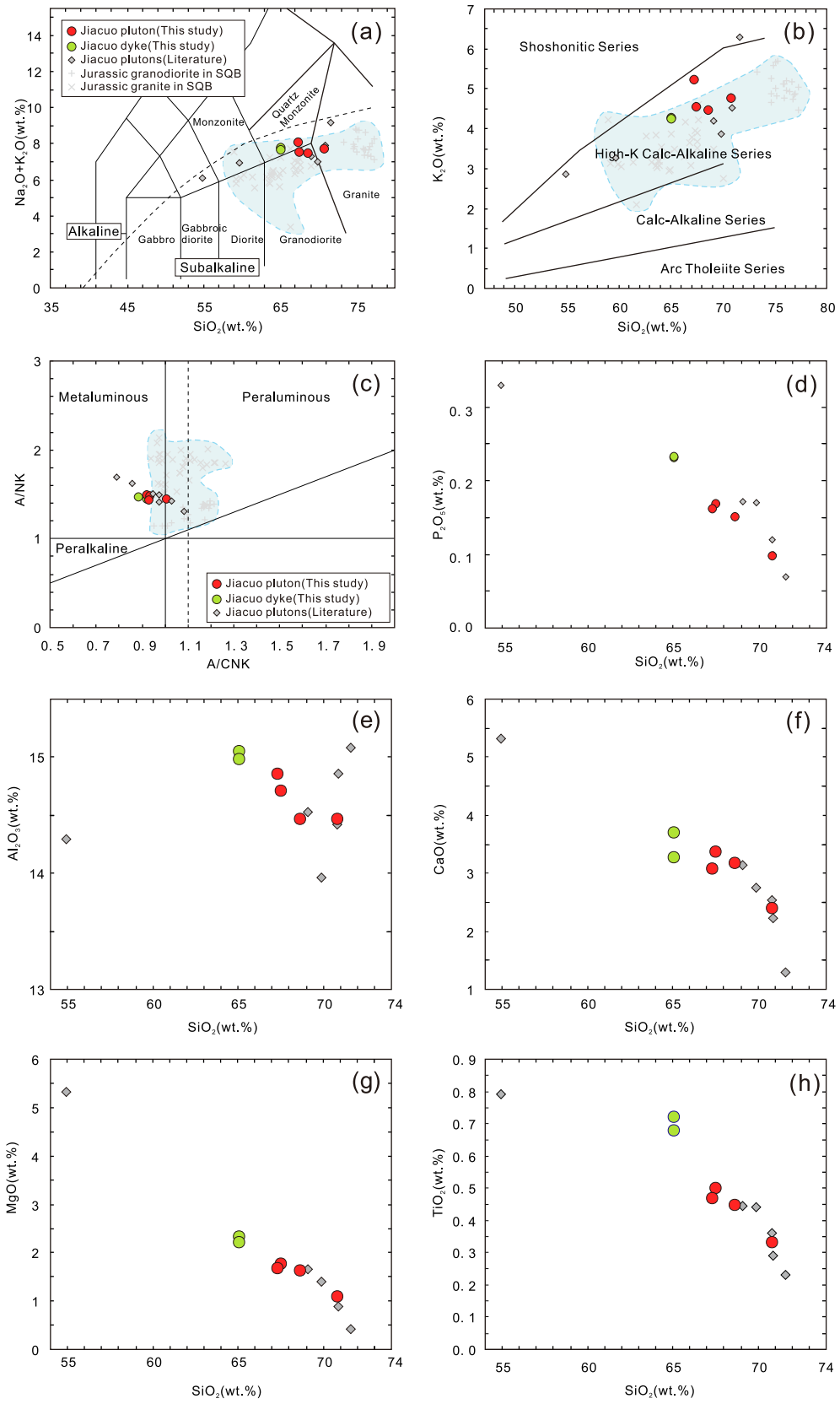


**Fig. 4.** (a) TAS classification diagram (Middlemost, 1994). (b) $K_2O$ versus $SiO_2$ diagram (Peccerillo and Taylor, 1976). (c) A/NK versus A/CNK diagram. (d–h) Harker diagrams. Data sources: Jiacuo granodiorite data from the literature are from Li et al. (2014a); Jurassic granodiorites in the SQB are from Li et al. (2014a, b), Liu et al. (2014a), and Wu et al. (2016); Jurassic granodiorites in the SQB are from Li et al. (2014a) and Liu et al. (2014a).

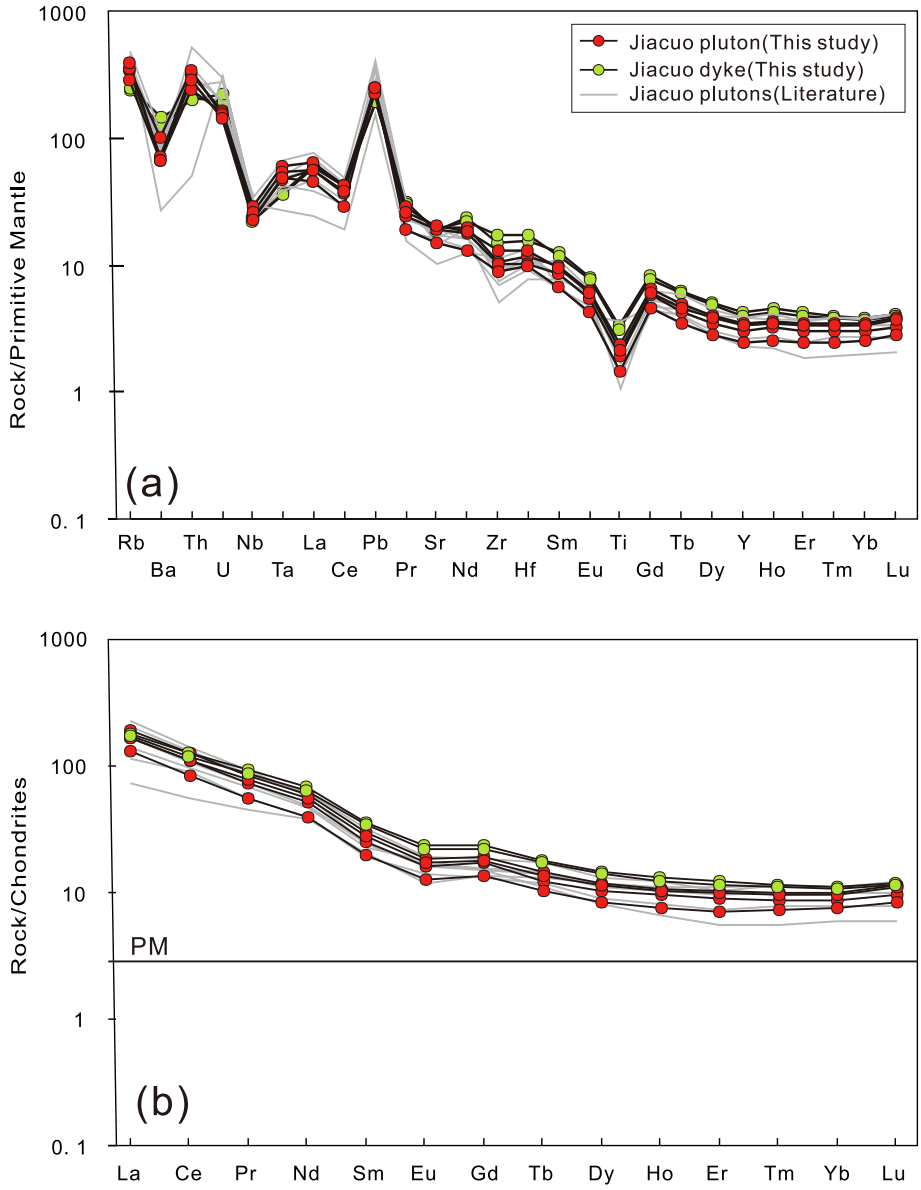


**Fig. 5.** Primitive mantle normalized trace elements (a) and chondrite normalized REEs (b) diagrams for the Jiacuo granodioritic intrusive rocks. Chondrite and primitive-mantle normalization values are from Sun and McDonough (1989). Jiacuo granodiorite data (literature) are from Li et al. (2014a).

dehydration melting of tholeiitic amphibolites are usually low in $K_2O$ ($Na_2O/K_2O > 1$) (Rapp and Watson, 1995; Rushmer, 1991), whereas all of the Jiacuo granodiorite samples show $Na_2O/K_2O < 1.0$ ($Na_2O/K_2O = 0.6–0.8$). Second, magmas derived from subducted mélange usually react with mantle-wedge peridotite during magma ascent, resulting in relatively high MgO contents (Hao et al., 2016b). However, the Jiacuo granodiorites have lower MgO contents (1.6–2.3 wt%) compared with those of subducted-mélange-derived magmas (2.5–4.7 wt%).

The high $K_2O$ contents and low MgO contents and $Mg^{\#}$ values of the Jiacuo granodiorites and dikes are similar to those of lower-crust-derived felsic melts (Li et al., 2014b; Hao et al., 2016b; Wu et al., 2016). The studied rocks have enriched whole-rock Sr–Nd and zircon Hf–O isotopic compositions, as well as ancient two-stage Nd ($T_{2DM}$, 1.6 Ga) and Hf ($T_{2DM}$, 1.7–2.1 Ga) model ages, indicating that they were derived by partial melting of ancient mafic lower crust rather than newly formed basaltic lower crust.

### 5.2. Late Mesozoic geodynamic processes in the southern Qiangtang Block

The closure age of the Bangong–Nujiang Tethyan Ocean is debated, and the collision of the southern Qiangtang and northern Lhasa blocks is thought to have occurred during the Middle Jurassic or the Early or Late Cretaceous (Chen et al., 2017; Geng et al., 2016; Guynn et al., 2006; Hao et al., 2016a, 2016b; Kapp et al., 2005; Leier et al., 2007; Li et al., 2018; Ma et al., 2017; Murphy et al., 1997; Otofuji et al., 2007;

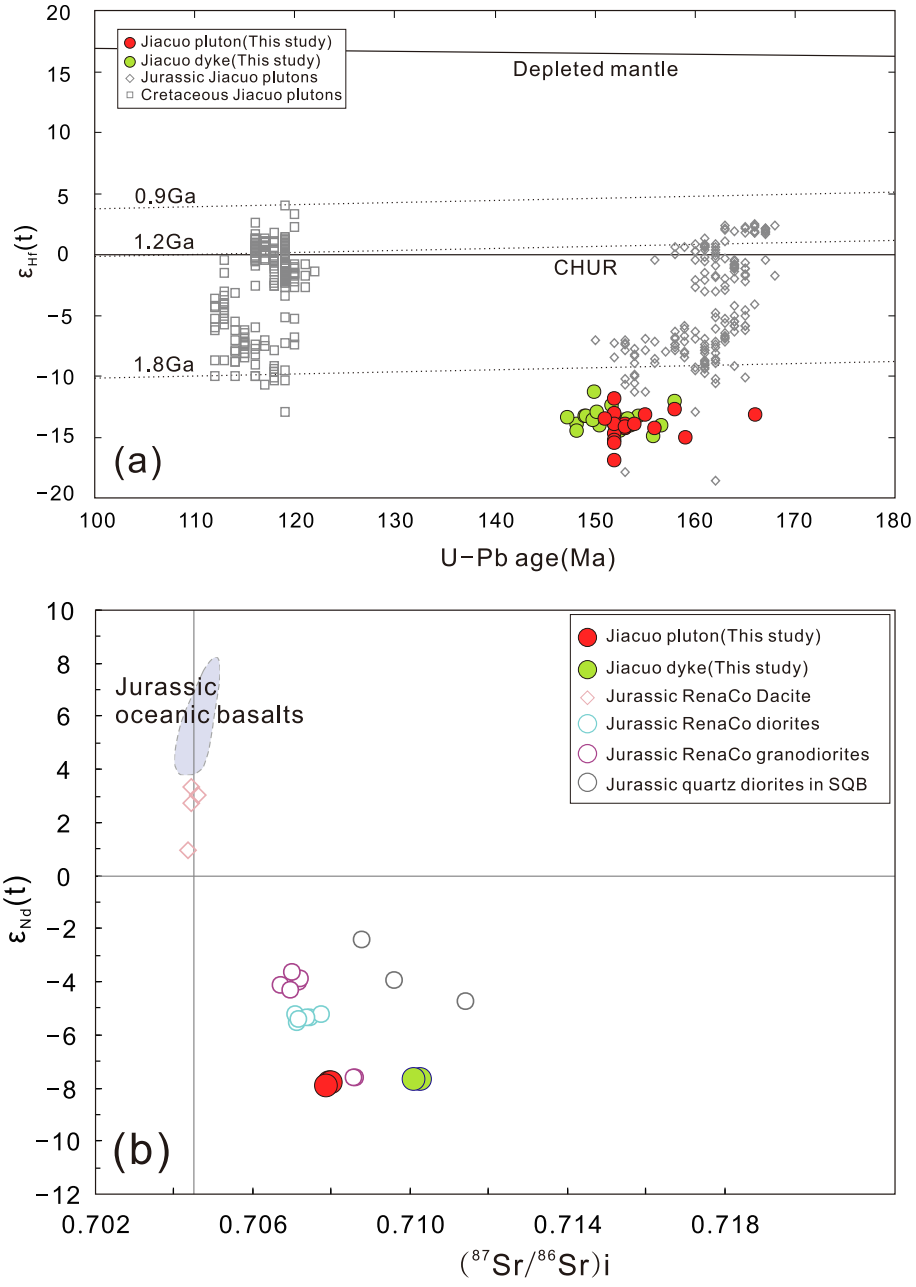


**Fig. 6.** (a) $\varepsilon_{Hf}(t)$ versus age diagram for late Mesozoic magmatic rocks in the Jiacuo area. The sub-horizontal lines depict Hf "crustal" model ages (TCDM), which were calculated by assuming that the parental magma was derived from an average continental crust (with $^{176}Lu/^{177}Hf$ = 0.015) that originated from a depleted mantle source Griffin et al., 2002. Data for the Jurassic Jiacuo granodiorites and the Cretaceous felsic intrusive rocks are from Li et al. (2014a). (b) $\varepsilon_{Nd}(t)$ versus $(^{87}Sr/^{86}Sr)_i$ diagram. Data sources: Jurassic Rena Co dacites are from Li et al. (2016b); Jurassic Rena Co granodiorites are from Hao et al. (2016a); quartz diorites are from Liu et al. (2014a); Jurassic oceanic basalts are from Bao et al. (2007), Zhang et al. (2014), and Zhu et al. (2006).

Schneider et al., 2003; Volkmer et al., 2007, 2014; Zhu et al., 2016). Therefore, the possibility that the southern margin of the SQB was in an arc setting during the Late Jurassic needs to be further clarified.

We suggest that the southern margin of the SQB belonged to the stage of arc magmatism rather than to the stage of post-collision during the Jurassic, according to the following lines of evidence. (1) The youngest ophiolites indicate that the Bangong–Nujiang Tethyan Ocean survived at least until the Middle Jurassic. In the Bangong–Nujiang Suture Zone, the ages of gabbro in ophiolites range from 188 to 162 Ma (Wang et al., 2016). Previous dating results for cumulate gabbros in ophiolite from the Rutog area show ages in the range 169–162 Ma (161.5 Ma, Liu et al., 2014b; 1650.5 and 169 Ma, Wang et al., 2016). (2) Late Mesozoic (169–148 Ma) magmatism in the SQB exhibits a northward migration trend, which can be explained by normal subduction rather than slab break-off (Li et al., 2018). The earliest (~169 Ma) igneous rocks in the SQB are granites and granodiorites in the Larelaxin and Labu Co–Rena Co areas (Li et al., 2014b; Liu et al., 2014a; Wu et al., 2016) and are confined to areas adjacent to the Bangong–Nujiang suture zone. Subsequently, magmatism started in the central SQB, including in the Qingcaoshan (~164 Ma; Li et al., 2014a),

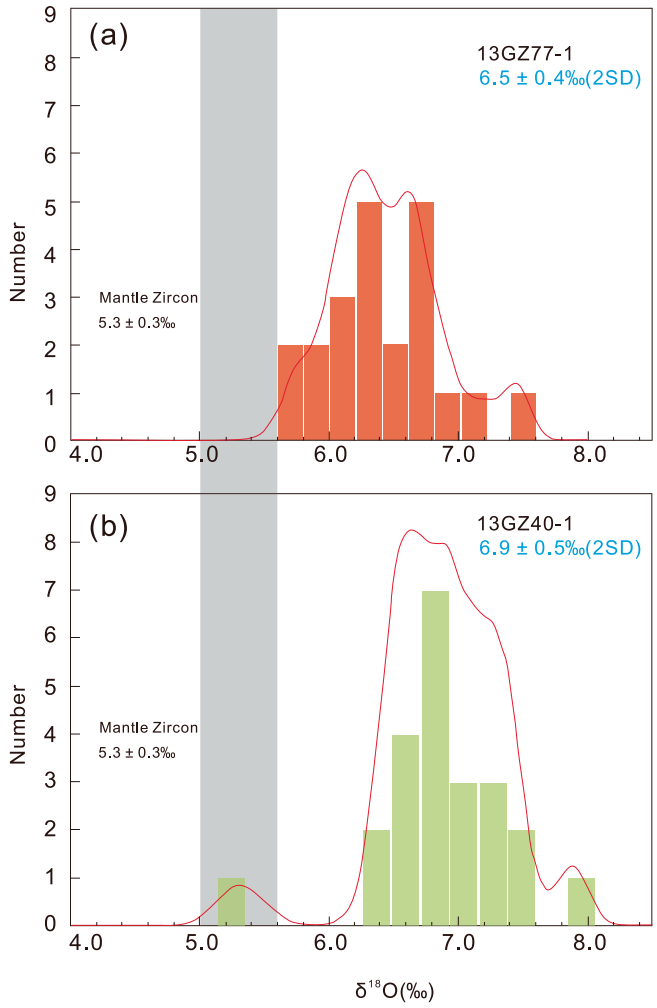


**Fig. 7.** Histogram of zircon $\delta^{18}O$ values. The gray field shows the $\delta^{18}O$ range for mantle zircons (Valley et al., 1998).

Xianqian (~161 Ma; Li et al., 2014a), and Jiacuo (~153 Ma; Li et al., 2014a; this study) areas. (3) Some igneous rock types indicate a geodynamic setting of subduction during the Jurassic. These include adakitic dacites (154 Ma; Li et al., 2016a) that formed by partial melting of oceanic crust in the SQB, and high-Mg andesites derived from subducted oceanic crust (162 Ma; Zeng et al., 2016) in the northern Lhasa Block, both of which indicate an oceanic subduction setting. Early Cretaceous (110–104 Ma) adakites and associated Nb-enriched basalts at Gerze may also indicate a subduction setting (Hao et al., 2018). Thus, these three lines of evidence together indicate that the southern margin of the SQB was in a continental margin arc setting during the Jurassic.

Two distinct magmatic episodes during the late Mesozoic have been identified in the SQB from a collation of published zircon ages of plutons (Hao et al., 2016a; Li et al., 2014a; b; Liu et al., 2017). It is difficult to fully evaluate U–Pb zircon age distributions in cases where the volumes of different magmatic rocks are uncertain. In consideration of this, we adopted the areas of the present-day exposures of granitic rocks as reflecting the original magma volumes and compiled these data in a histogram of exposed area of late Mesozoic plutons with their zircon ages (Fig. 8). The plot shows an obvious gap in magmatism in the SQB during the late Mesozoic (148–122 Ma). This gap is thought to have been caused by flat subduction of the Bangong–Nujiang Tethyan oceanic slab (Geng et al., 2016; Hao et al., 2016a; Li et al., 2018), as inferred from the features and patterns of magmatism and associated metallogenesis. Geng et al. (2016) suggested that the low-density and thickened (> 10 km) subducting Bangong–Nujiang Tethyan oceanic slab favored the occurrence of low-angle to flat subduction. The earliest magmatic rocks related to Bangong–Nujiang Tethyan oceanic slab subduction in the SQB are the Jurassic granites of the Larelaxin and Caima plutons (~168 Ma; Li et al., 2014b), which are close to the Bangong–Nujiang suture zone. Subsequently, the subduction-related magmatism became more widespread and extended farther inland (Fig. 1). The arc magmatism migrated landward before the magmatic lull, probably owing to a shallowing in the angle of subduction of the Bangong–Nujiang Tethyan oceanic slab.

Given the above discussion, we present a model of the tectono-magmatic evolution of the SQB during the Mesozoic, as follows (Fig. 9).

(1) During the Middle Jurassic (~170 Ma), the Bangong–Nujiang Tethyan oceanic slab was subducted northward beneath the SQB. At this time, the magmatic arc was located close to the trench. Underplating of the lower crust of the SQB by mantle-derived basaltic melts caused dehydration melting of the ancient lower crust. Quartz diorites and granodiorites (168 Ma) in the Larelaxin and Labu Co areas were generated by dehydration melting of ancient lower crust with a minor contribution from mantle-derived mafic components.
(2) During the Middle to Late Jurassic (168–148 Ma), the magmatism gradually migrated far away from the trench in the SQB. The generation of the northernmost Jiacuo granodiorites during the Late Jurassic (153–152 Ma) probably reflected a shallowing in the subduction angle of the Bangong–Nujiang Tethyan oceanic plate, with the magma-generating portion of the slab being distant from the trench. Subsequently, the continuing northward flat subduction of the Bangong–Nujiang oceanic slab led to a magmatic lull during 148–122 Ma.

## 6. Conclusions

(1) The Jiacuo granodiorites and dikes, which are located in the northernmost SQB, were emplaced during 153–152 Ma and were most probably derived by partial melting of ancient mafic lower crust.
(2) During the Jurassic, the southern margin of the SQB was in a continental margin arc setting and contained ancient crustal basement.
(3) Late Jurassic magmatism in the SQB most probably resulted from northward subduction of the Bangong–Nujiang Tethyan oceanic slab.

## CRediT authorship contribution statement

**Peng Sun:** Conceptualization, Formal analysis, Writing - original draft, Visualization. **Wei Dan:** Investigation, Resources, Writing - review & editing, Project administration. **Qiang Wang:**

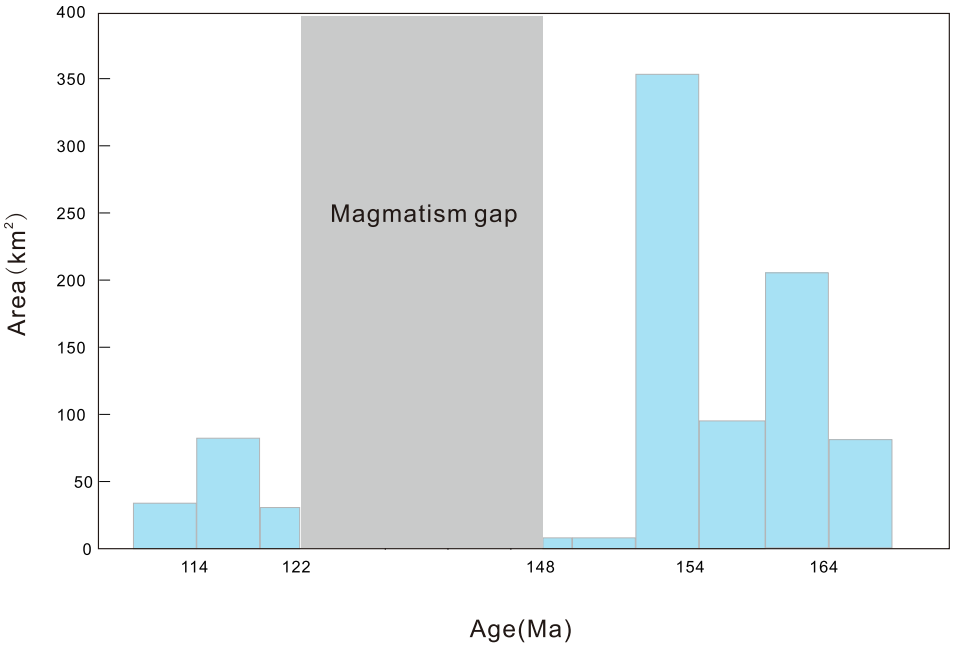


**Fig. 8.** Histogram of the exposed area of late Mesozoic plutons.

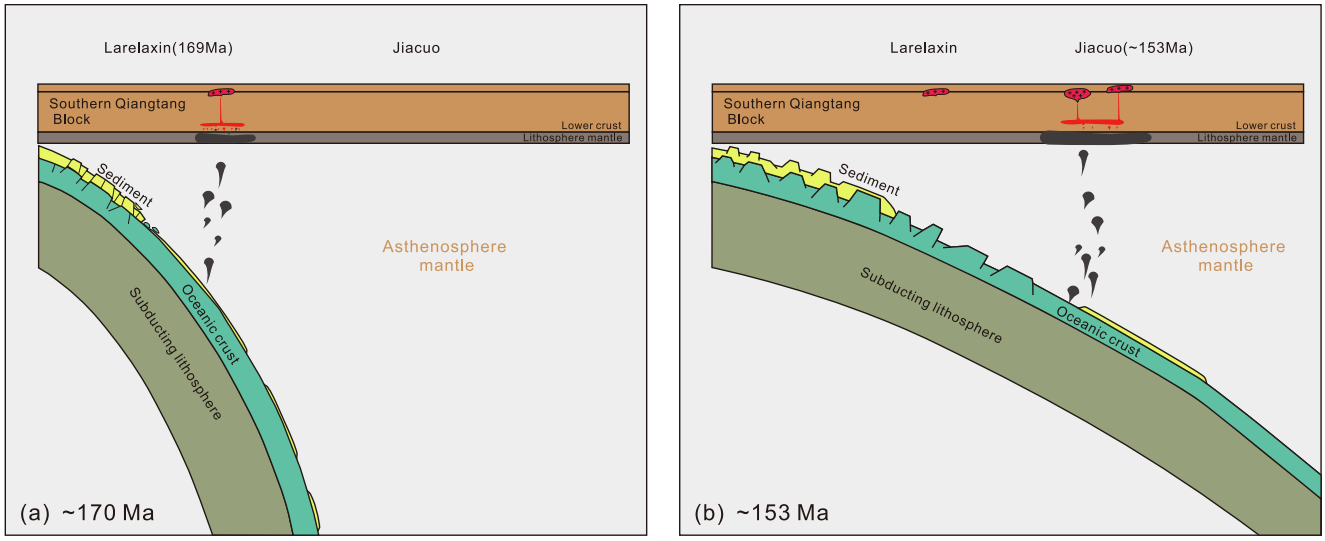


**Fig. 9.** Conceptual model illustrating the tectonic and magmatic evolution of central Tibet during the late Mesozoic (this cartoon is not to real scale). See the text for detail.

Conceptualization, Writing - review & editing, Supervision, Project administration. **Gong-Jian Tanga:** Writing - review & editing. **Quan Ou:** Investigation. **Lu-Lu Hao:** Investigation. **Zi-Qi Jiang:** Investigation.

## Declaration of Competing Interest

The authors declare that they have no known competing financial interests or personal relationships that could have appeared to influence the work reported in this paper.

## Acknowledgments

We are grateful to Editor-in-Chief Professor Meifu Zhou and two anonymous reviewers for their critical reviews and constructive comments, which significantly improved the manuscript. We appreciate the assistance of Xiaoping Xia, Xianglin Tu, Shengling Sun, Xinyu Wang, and Le Zhang for the geochemical analyses. This work was supported by funding from the National Key R&D Program of China (2016YFC0600407), the National Natural Science Foundation of China (grant nos. 91855215, 41722205, 41673033, 41630208, and 41673033), the Second Tibetan Plateau Scientific Expedition and Research (STEP) (2019QZKK0702), the Key Program of the Chinese Academy of Sciences (QYZDJ–SSW–DQC026), the Key Science Program of Guangzhou City, China (201707020032), and the Guangzhou Institute of Geochemistry of the Chinese Academy of Sciences (GIGCAS 135 Project [135TP201601]). This is contribution No. IS-2808 from GIG–CAS.

## Appendix A. Supplementary material

Supplementary data to this article can be found online at https://doi.org/10.1016/j.jseaes.2020.104235.

## References


Altherr, R., Holl, A., Hegner, E., Langer, C., Kreuzer, H., 2000. High-potassium, calc-alkaline I-type plutonism in the European Variscides: northern Vosges (France) and northern Schwarzwald (Germany). Lithos 50, 51–73.

Andersen, T., 2002. Correction of common lead in U-Pb analyses that do not report 204Pb. Chem. Geol. 192, 59–79.

Bao, P.S., Xiao, X.C., Su, L., Wang, J., 2007. Petrological, geochemical and chronological constraints for the tectonic setting of the Dongco ophiolite in Tibet. Sci. China, Ser. D Earth Sci. 50, 660–671 (in Chinese with English abstract).

Beard, J.S., Lofgren, G.E., 1991. Dehydration melting and water-saturated melting of basaltic and andesitic greenstones and amphibolites at 1, 3, and 6. 9 kb. J. Petrol. 32, 365–401.

Belousova, E., Griffin, W., O'Reilly, S.Y., Fisher, N., 2002. Igneous zircon: trace element composition as an indicator of source rock type. Contrib. Miner. Petrol. 143, 602–622.

Chappell, B.W., White, A.J., 2001. Two contrasting granite types: 25 years later. Aust. J. Earth Sci. 48, 489–499.

Chen, W., Zhang, S., Ding, J., Zhang, J., Zhao, X., Zhu, L., Yang, W., Yang, T., Li, H., Wu, H., 2017. Combined paleomagnetic and geochronological study on Cretaceous strata of the Qiangtang terrane, central Tibet. Gondwana Res. 41, 373–389.

Chu, M.F., Chung, S.L., Song, B., Liu, D.Y., O'Reilly, S.Y., Pearson, N.J., Ji, J.Q., Wen, D.J., 2006. Zircon U–Pb and Hf isotope constraints on the Mesozoic tectonics and crustal evolution of southern Tibet. Geology 34, 745–748.

Chung, S.L., Chu, M.F., Zhang, Y., Xie, Y., Lo, C.H., Lee, T.Y., Lan, C.Y., Li, X., Zhang, Q., Wang, Y., 2005. Tibetan tectonic evolution inferred from spatial and temporal variations in post-collisional magmatism. Earth-Sci. Rev. 68, 173–196.

Dan, W., Wang, Q., White, W.M., Zhang, X.Z., Tang, G.J., Jiang, Z.Q., Hao, L.L., Ou, Q., 2018a. Rapid formation of eclogites during a nearly closed ocean: Revisiting the Pianshishan eclogite in Qiangtang, central Tibetan Plateau. Chem. Geol. 477, 112–122.

Dan, W., Wang, Q., Zhang, X.Z., Zhang, C., Tang, G.-J., Wang, J., Ou, Q., Hao, L.L., Qi, Y., 2018b. Magmatic record of Late Devonian arc-continent collision in the northern Qiangtang, Tibet: Implications for the early evolution of East Paleo-Tethys Ocean. Lithos 308, 104–117.

Geng, Q.R., Zhang, Z., Peng, Z.M., Guan, J.L., Zhu, X.P., Mao, X.C., 2016. Jurassic-Cretaceous granitoids and related tectono-metallogenesis in the Zapug-Duobuza arc, western Tibet. Ore Geol. Rev. 77, 163–175.

Griffin, W.L., Wang, X., Jackson, S.E., Pearson, N.J., O'Reilly, S.Y., Xu, X.S., Zhou, X.M., 2002. Zircon chemistry and magma mixing, SE China: in-situ analysis of Hf isotopes, Tonglu and Pingtan igneous complexes. Lithos 61, 237–269.

Grove, T.L., Donnelly-Nolan, J.M., Housh, T., 1997. Magmatic processes that generated the rhyolite of Glass Mountain, Medicine Lake volcano, N. California. Contrib. Mineral. Petrol. 127, 205–223.

Guynn, J.H., Kapp, P., Pullen, A., Heizler, M., Gehrels, G., Ding, L., 2006. Tibetan basement rocks near Amdo reveal "missing" Mesozoic tectonism along the Bangong suture, central Tibet. Geology 34, 505–508.

Hao, L.L., Wang, Q., Zhang, C., Ou, Q., Yang, J.H., Dan, W., Jiang, Z.Q., 2018. Oceanic plateau subduction during closure of the Bangong-Nujiang Tethyan Ocean: Insights from central Tibetan volcanic rocks. Geol. Soc. Am. Bull. 131, 864–880.

Hao, L.L., Wang, Q., Wyman, D.A., Ou, Q., Dan, W., Jiang, Z.Q., Wu, F.Y., Yang, J.H., Long, X.P., Li, J., 2016a. Underplating of basaltic magmas and crustal growth in a continental arc: Evidence from Late Mesozoic intermediate–felsic intrusive rocks in southern Qiangtang, central Tibet. Lithos 245, 223–242.

Hao, L.L., Wang, Q., Wyman, D.A., Ou, Q., Dan, W., Jiang, Z.Q., Yang, J.H., Li, J., Long, X.P., 2016b. Andesitic crustal growth via mélange partial melting: Evidence from Early Cretaceous arc dioritic/andesitic rocks in southern Qiangtang, central Tibet. Geochem. Geophys. Geosyst. 17, 1641–1659.

He, W., Yang, L., Lu, Y., Jeon, H., Xie, S., Gao, X., 2018. Zircon U-Pb dating, geochemistry and Sr–Nd–Hf–O isotopes for the Baimaxueshan granodiorites and mafic microgranulars enclaves in the Sanjiang Orogen: Evidence for westward subduction of Paleo-Tethys. Gondwana Res. 62, 112–126.

Jin, X.C., 2002. Permo-Carboniferous sequences of Gondwana affinity in southwest China and their paleogeographic implications. J. Asian Earth Sci. 20, 633–646.

Kapp, P., Murphy, M.A., Yin, A., Harrison, T.M., Ding, L., Guo, J., 2003. Mesozoic and Cenozoic tectonic evolution of the Shiquanhe area of western Tibet. Tectonics 22.

Kapp, P., Yin, A., Harrison, T.M., Ding, L., 2005. Cretaceous-Tertiary shortening, basin development, and volcanism in central Tibet. Geol. Soc. Am. Bull. 117, 865–878.

Kapp, P., Yin, A., Manning, C.E., Murphy, M., Harrison, T.M., Spurlin, M., Lin, D., Deng, X.G., Wu, C.M., 2000. Blueschist-bearing metamorphic core complexes in the Qiangtang block reveal deep crustal structure of northern Tibet. Geology 28, 19–22.

Leier, A.L., Decelles, P.G., Kapp, P., Gehrels, G.E., 2007. Lower Cretaceous Strata in the Lhasa Terrane, Tibet, with Implications for Understanding the Early Tectonic History of the Tibetan Plateau. J. Sediment. Res. 77, 809–825.

Li, C., Cheng, L.R., Hu, K., Yang, Z.R., Hong, Y.R., 1995. Study on the Paleo-Tethys Suture Zone of Longmu Co-Shuanghu, Tibet (in Chinese with English abstract). Geological House, Beijing.

Li, G.M., Li, J.X., Qin, K.Z., Duo, J., Zhang, T.P., Xiao, B., Zhao, J.X., 2012. Geology and hydrothermal alteration of the duobuza gold-rich porphyry copper district in the bangongco metallogenetic belt, northwestern tibet. Resour. Geol. 62, 99–118.

Li, G.M., Qin, K.Z., Li, J.X., Evans, N.J., Zhao, J.X., Cao, M.J., Zhang, X.N., 2015. Cretaceous magmatism and metallogeny in the Bangong-Nujiang metallogenic belt, central Tibet: Evidence from petrogeochemistry, zircon U-Pb ages, and Hf–O isotopic compositions. Gondwana Res. 41, 110–127.

Li, J.X., Qin, K.Z., Li, G.M., Richards, J.P., Zhao, J.X., Cao, M.J., 2014a. Geochronology, geochemistry, and zircon Hf isotopic compositions of Mesozoic intermediate–felsic intrusions in central Tibet: Petrogenetic and tectonic implications. Lithos 198, 77–91.

Li, J.X., Qin, K.Z., Li, G.M., Xiao, B., Zhao, J.X., Cao, M.J., Chen, L., 2013. Petrogenesis of ore-bearing porphyries from the Duolong porphyry Cu–Au deposit, central Tibet: Evidence from U-Pb geochronology, petrochemistry and Sr–Nd–Hf–O isotope characteristics. Lithos 160, 216–227.

Li, S.M., Zhu, D.C., Wang, Q., Zhao, Z., Zhang, L.L., Liu, S.A., Chang, Q.-S., Lu, Y.H., Dai, J.G., Zheng, Y.C., 2016a. Slab-derived adakites and subslab asthenosphere-derived OIB-type rocks at 156 ± 2 Ma from the north of Gerze, central Tibet: Records of the Bangong-Nujiang oceanic ridge subduction during the Late Jurassic. Lithos 262, 456–469.

Li, S.M., Zhu, D.C., Wang, Q., Zhao, Z.D., Sui, Q.L., Liu, S.A., Liu, D., Mo, X.X., 2014b. Northward subduction of Bangong-Nujiang Tethys: Insight from Late Jurassic intrusive rocks from Bangong Tso in western Tibet. Lithos 205, 284–297.

Li, X.H., Li, Z.X., Li, W.X., Liu, Y., Yuan, C., Wei, G., Qi, C., 2007. U-Pb zircon, geochemical and Sr–Nd–Hf isotopic constraints on age and origin of Jurassic I-and A-type granites from central Guangdong, SE China: a major igneous event in response to foundering of a subducted flat-slab? Lithos 96, 186–204.

Li, X.K., Chen, J., Wang, R.C., Li, C., 2018. Temporal and spatial variations of Late Mesozoic granitoids in the SW Qiangtang, Tibet: Implications for crustal architecture, Meso-Tethyan evolution and regional mineralization. Earth Sci. Rev. 185, 374–396.

Li, X.H., Li, Z.X., Wingate, M.T.D., Chung, S.L., Liu, Y., Lin, G.C., Li, W.X., 2006. Geochemistry of the 755 Ma Mundine Well dyke swarm, northwestern Australia: Part of a Neoproterozoic mantle superplume beneath Rodinia? Precambr. Res. 146, 1–15.

Li, X.H., Long, W.G., Li, Q.L., Liu, Y., Zheng, Y.F., Yang, Y.H., Chamberlain, K.R., Wan, D. F., Guo, C.H., Wang, X.C., 2010. Li X H, Long W G, Li Q L, et al. Penglai zircon megacrysts: a potential new working reference material for microbeam determination of Hf–O isotopes and U–Pb age. Geostandards Geoanalyt. Res. 34, 117–134.

Li, X.K., Li, C., Sun, Z.M., Wang, M., 2016b. Origin and tectonic setting of the giant Duolong Cu–Au deposit, South Qiangtang Terrane, Tibet: Evidence from geochronology and geochemistry of Early Cretaceous intrusive rocks. Ore Geol. Rev. 80, 61–78.

Liu, D.L., Huang, Q.S., Fan, S.Q., Zhang, L.Y., Shi, R.D., Ding, L., 2014a. Subduction of the Bangong-Nujiang Ocean: constraints from granites in the Bangong Co area. Tibet. Geol. J. 49, 188–206.

Liu, D.L., Shi, R.D., Ding, L., Huang, Q.S., Zhang, X.R., Yue, Y.H., Zhang, L.Y., 2017. Zircon U–Pb Age and Hf Isotopic Compositions of Mesozoic Granitoids in Southern Qiangtang, Tibet: Implications for the Subduction of the Bangong–Nujiang Tethyan Ocean. Gondwana Res. 41, 157–172.

Liu, W.L., Xia, B., Zhong, Y., Cai, J.X., Li, J.F., Liu, H.F., Cai, Z.R., Sun, Z.L., 2014b. Age and composition of the Rebang Co and Julu ophiolites, central Tibet: Implications for the evolution of the Bangong Meso-Tethys. Int. Geol. Rev. 56, 430–447.

Liu, Y., Gao, S., Hu, Z., Gao, C., Zong, K., Wang, D., 2010. Continental and oceanic crust recycling-induced melt-peridotite interactions in the trans-north China Orogen: U-Pb dating, Hf isotopes and trace elements in zircons from mantle xenoliths. J. Petrol. 51, 392–399.

Ludwig, K.R., 2003. User'smanual for Isoplot 3.00: a geochronological toolkit for Microsoft Excel. Kenneth R. Ludwig.

Ma, A., Hu, X., Garzanti, E., Han, Z., Lai, W., 2017. Sedimentary and tectonic evolution of the southern Qiangtang basin: Implications for the Lhasa-Qiangtang collision timing. J. Geophys. Res. Solid Earth 122, 4790–4813.

Metcalfe, I., 2002. Permian tectonic framework and palaeogeography of SE Asia. J. Asian Earth Sci. 20, 551–566.

Metcalfe, I., 2013. Gondwana dispersion and Asian accretion: Tectonic and palaeogeographic evolution of eastern Tethys. J. Asian Earth Sci. 66, 1–33.

Middlemost, E.A., 1994. Naming materials in the magma/igneous rock system. Earth Sci. Rev. 37, 215–224.

Murphy, M.A., Yin, A., Harrison, T.M., Dürr, S.B., Chen, Z., Ryerson, F.J., Kidd, W.S.F., Wang, X., Zhou, X., 1997. Did the Indo-Asian collision alone create the Tibetan plateau? Geology 25, 719–722.

Otofuji, Y.I., Mu, C.L., Tanaka, K., Miura, D., Inokuchi, H., Kamei, R., Tamai, M., Takemoto, K., Zaman, H., Yokoyama, M., 2007. Spatial gap between Lhasa and Qiangtang blocks inferred from Middle Jurassic to Cretaceous paleomagnetic data. Earth Planet. Sci. Lett. 262, 581–593.

Peccerillo, A., Taylor, S., 1976. Geochemistry of Eocene calc-alkaline volcanic rocks from the Kastamonu area, northern Turkey. Contrib. Miner. Petrol. 58, 63–81.

Petford, N., Atherton, M., 1996. Na-rich partial melts from newly underplated basaltic crust: the Cordillera Blanca Batholith, Peru. J. Petrol. 37, 1491–1521.

Pullen, A., Kapp, P., Gehrels, G.E., Ding, L., Zhang, Q., 2011. Metamorphic rocks in central Tibet: Lateral variations and implications for crustal structure. Geol. Soc. Am. Bull. 123, 585–600.

Rapp, R.P., Watson, E.B., 1995. Dehydration melting of metabasalt at 8–32 kbar: implications for continental growth and crust-mantle recycling. J. Petrol. 36, 891–931.

Rushmer, T., 1991. Partial melting of two amphibolites: contrasting experimental results under fluid-absent conditions. Contrib. Miner. Petrol. 107, 41–59.

Schneider, W., Mattern, F., Wang, P.J., Li, C., 2003. Tectonic and sedimentary basin evolution of the eastern Bangong-Nujiang zone (Tibet): a Reading cycle. Int. J. Earth Sci. 92, 228–254.

Sun, S.S., McDonough, W.F., 1989. Chemical and isotopic systematics of oceanic basalts: implications for mantle composition and processes. Geol. Soc., London, Special Publ. 42, 313–345.

Valley, J.W., Kinny, P.D., Schulze, D.J., Spicuzza, M.J., 1998. Zircon megacrysts from kimberlite: oxygen isotope variability among mantle melts. Contrib. Miner. Petrol. 133, 1–11.

Volkmer, J.E., Kapp, P., Guynn, J.H., Lai, Q., 2007. Cretaceous-Tertiary structural evolution of the north central Lhasa terrane. Tibet. Tectonics 26.

Volkmer, J.E., Kapp, P., Horton, B.K., Gehrels, G.E., Minervini, J.M., Lin, D., 2014. Northern Lhasa thrust belt of central Tibet: Evidence of Cretaceous-early Cenozoic shortening within a passive roof thrust system? Geol. Soc. Am. Special Papers 507, 59–70.

Wang, B.D., Wang, L.Q., Chung, S.L., Chen, J.L., Yin, F.G., Liu, H., Li, X.B., Chen, L.K., 2016. Evolution of the Bangong-Nujiang Tethyan ocean: Insights from the geochronology and geochemistry of mafic rocks within ophiolites. Lithos 245, 18–33.

Wedepohl, K., 1991. Chemical composition and fractionation of the continental crust. Geol. Rundsch. 80, 207–223.

Wiedenbeck, M., Allé, P., Corfu, F., Griffin, W.L., Meier, M., Oberli, F., Quadt, A.V., Roddick, J.C., Spiegel, W., 1995. Three natural zircon standards for U-Th-Pb, Lu-Hf, trace element and REE analyses. Geostand. Geoanal. Res. 19, 1–23.

Wu, F.Y., Jahn, B.M., Wilde, S.A., Lo, C.H., Yui, T.F., Lin, Q., Ge, W.C., Sun, D.Y., 2003. Highly fractionated I-type granites in NE China (I): geochronology and petrogenesis. Lithos 66, 241–273.

Wu, H., Xie, C., Li, C., Wang, M., Fan, J., Xu, W., 2016. Tectonic shortening and crustal thickening in subduction zones: Evidence from Middle-Late Jurassic magmatism in Southern Qiangtang, China. Gondwana Res. 39, 1–13.

Xie, L.W., Zhang, Y.B., Zhang, H.H., Sun, J.F., Wu, F.Y., 2008. In situ simultaneous determination of trace elements, U-Pb and Lu-Hf isotopes in zircon and baddeleyite. Chin. Sci. Bull. 53, 1565–1573.

Yang, L.Q., Deng, J., Dilek, Y., Qiu, K.F., Ji, X.Z., Li, N., Taylor, R.D., Yu, J.Y., 2015. Structure, geochronology, and petrogenesis of the Late Triassic Puziba granitoid dikes in the Mianlue suture zone, Qinling orogeny,China. Bulletin 127, 1831–1854.

Yin, A., Harrison, T.M., 2000. Geologic evolution of the himalayan-tibetan orogen. Annu. Rev. Earth Planet. Sci. 28, 211–280.

Yu, Y.P., Xie, C.M., Fan, J.J., Wang, M., Dong, Y.C., Wang, B., Hao, Y.J., 2018. Zircon U-Pb geochronology and geochemistry of Early Jurassic granodiorites in Sumdo area, Tibet: Constraints on petrogenesis and the evolution of the Neo-Tethyan Ocean. Lithos 320–321, 134–143.

Zeng, Y.C., Chen, J.L., Xu, J.F., Wang, B.D., Huang, F., 2016. Sediment melting during subduction initiation: Geochronological and geochemical evidence from the Darutso high-Mg andesites within ophiolite melange, central Tibet. Geochem. Geophys. Geosyst. 17, 4859–4877.

Zhai, Q.G., Jahn, B.M., Su, L., Wang, J., Mo, X.X., Lee, H.Y., Wang, K.L., Tang, S., 2013. Triassic arc magmatism in the Qiangtang area, northern Tibet: Zircon U-Pb ages, geochemical and Sr–Nd–Hf isotopic characteristics, and tectonic implications. J. Asian Earth Sci. 63, 162–178.

Zhai, Q.G., Zhang, R.Y., Jahn, B.M., Li, C., Song, S.G., Wang, J., 2011. Triassic eclogites from central Qiangtang, northern Tibet, China: petrology, geochronology and metamorphic P-T path. Lithos 125, 173–189.

Zhang, K.J., Cai, J.X., Zhang, Y.X., Zhao, T.P., 2006. Eclogites from central Qiangtang, northern Tibet (China) and tectonic implications. Earth Planet. Sci. Lett. 245, 722–729.

Zhang, K.J., Zhang, Y.X., Tang, X.C., Xia, B., 2012. Late Mesozoic tectonic evolution and growth of the Tibetan plateau prior to the Indo-Asian collision. Earth Sci. Rev. 114, 236–249.

Zhang, L., Ren, Z.Y., Nichols, A.R., Zhang, Y.H., Zhang, Y., Qian, S.-P., Liu, J.Q., 2014. Lead isotope analysis of melt inclusions by LA-MC-ICP-MS. J. Anal. At. Spectrom. 29, 1393–1405.

Zhang, X.Z., Dong, Y.S., Wang, Q., Dan, W., Zhang, C., Deng, M.R., Xu, W., Xia, X.P., Zeng, J.P., Liang, H., 2016. Carboniferous and Permian evolutionary records for the Paleo-Tethys Ocean constrained by newly discovered Xiangtaohu ophiolites from central Qiangtang, central Tibet. Tectonics 35, 1670–1686.

Zhao, Z., Bons, P.D., Wang, G., Liu, Y., Zheng, Y., 2014. Origin and pre-Cenozoic evolution of the south Qiangtang basement, Central Tibet. Tectonophysics 623, 52–66.

Zhu, D.C., Pan, G.T., Mo, X.X., Wang, L.Q., Zhao, Z.D., Liao, Z.L., Geng, Q.R., Dong, G.C., 2006. Identification for the Mesozoic OIB-type basalts in central Qinghai-Tibetan Plateau: geochronology, geochemistry and their tectonic setting. Acta Geol. Sin. 80, 1312–1328 (in Chinese with English abstract).

Zhu, D.C., Zhao, Z.D., Niu, Y., Dilek, Y., Hou, Z.Q., Mo, X.X., 2013. The origin and pre-Cenozoic evolution of the Tibetan Plateau. Gondwana Res. 23, 1429–1454.

Zhu, D.C., Li, S.M., Cawood, P.A., Wang, Q., Zhao, Z.D., Liu, S.A., Wang, L.Q., 2016. Assembly of the Lhasa and Qiangtang terranes in central Tibet by divergent double subduction. Lithos 245, 7–17.

Zhu, D.C., Zhao, Z.D., Niu, Y., Mo, X.X., Chung, S.L., Hou, Z.Q., Wang, L.Q., Wu, F.Y., 2011. The Lhasa Terrane: Record of a microcontinent and its histories of drift and growth. Earth Planet. Sci. Lett. 301, 241–255.